An advanced impedance calibration method for nanoscale microwave imaging

M. Kasper[1,*], G. Gramse[2] and F. Kienberger[1]

[1] Keysight Technologies Austria GmbH, Keysight Labs, Gruberstrasse 40, 4020 Linz, Austria
[2] Biophysics Institute, Johannes Kepler University of Linz, Gruberstrasse 40, 4020 Linz, Austria
* *Correspondence: manuel.kasper@keysight.com*

Abstract — We present a new calibration method for nanoscale complex impedance imaging with the scanning microwave microscope (SMM), which does not require any calibration samples. Instead, the vector network analyser (VNA) and the corresponding electronically switched calibration (ECal) capabilities in combination with time domain gating and microwave network modelling are used to de-embed the full system. Based on this workflow the measured complex reflection S11 signal can be directly split into the reactive (capacitive) and lossy (conductive) sample behavior. Nano Schottky diodes on a semiconductor substrate as well as biological cells were measured to demonstrate that the sample conductance and susceptance correspond directly to S11 amplitude and phase, respectively. We show fully calibrated capacitance and conductance images which result from the final step of the calibration workflow that applies tip-sample approach curves. This advanced workflow of quantitative impedance calibration can have various applications starting from semiconductor failure analysis to novel 2D materials and biological cells in liquid environment. Index Terms — Scanning microwave microscopy, reflection calibration, ECal, time domain gating, deembedding.

I. INTRODUCTION

Scanning Microwave Microscopy (SMM) allows characterizing electric and magnetic properties of materials at microwave frequencies with nanometer lateral resolution. SMM merges the nanoscale imaging of an atomic force microscope (AFM) with the high-frequency broadband (from MHz to GHz) impedance measurement capabilities of a vector network analyzer (VNA). In reflection SMM mode, the ratio of the reflected and incident electromagnetic waves, the so called S_{11} scattering parameter, is measured by the VNA at each AFM tip/sample contact point. In order to enhance the signal to noise ratio (SNR), typically an impedance matching network is used to connect the tip to the VNA. The tip (radius 10 – 500 nm) is scanning over the sample surface with constant tip-sample contact force. This is realized by a feedback loop in combination with optical deflection readout and a piezoelectric mechanical scanner. Applications are in the area of high and low loss material characterization [1], semiconductor dopant concentration measurements, device failure analysis [2, 3, 4] and measurements on biological samples [5, 6, 7]. Subsurface measurement capablities have been shown [8, 9]. Interferometric hardware improvements are presented in [10] and a review is given in [11]. In contrast to Scanning Capacitance Microscopy (SCM) that operates at a fixed frequency below 1 GHz, SMM is operating broadband at significantly higher frequencies of 1-20 GHz. In contrast to SCM, SMM can measure not only capacitance but allows to measure resistances as well. Various calibration procedures have been proposed to allow calibrated complex impedance measurements [12, 13]. All of these procedures require calibration capacitances at the tip, for example nanoscopic physical capacitors on a calibration sample. It also has been shown that the capacitance created by the tip apex and cone which varies with its distance to the sample can be used for calibration purposes employing additonal techniques [14, 15].

The new workflow described in this paper enables phase calibration without the need for nanoscopic calibration standards. This allows distinguishing between reactive (capacitive) and lossy (conductive) sample behavior. SMM cantilever approach curves are used to add amplitude calibration resulting in calibrated impedance values (i.e. conductance and capacitance). We apply the new calibration workflow to nano Schottky diode measurements resulting in fully calibrated capacitance and conductance images. Finally, the method is applied to biological cell measurements.

II. VNA REFLECTION CALIBRATION

In the well estabilished standard procedures for reflection calibration several calibration standards need to be connected to a network analyzers port to realize a proper calibration. Today electronically switchable calibration standards (ECal) with a single connector are available to facilitate this in a very reproducible way without cable movements etc. Moreover also two port units with a built in “Thru” standard exist [16].

Fig. 1 (a) shows the proposed system setting with the SMM cantilever and sample, a resonator cable for impedance matching, an ECal and a VNA. The quantity that actually should be measured is the complex tip admittance

$$Y_{tip} = G_{tip} + j\omega C_{tip} \qquad (1)$$

composed of conductivity G_{tip} and capacitance C_{tip} and ω being the angular frequency of the RF signal. It is important that the “Thru” standard is not lossless and also not perfectly matched which adds a discontinuity to the signal path. This is

This paper is an expanded version from the 2016 International Microwave Conference, San Francisco, CA, May 22-27, 2016

necessary for the correct operation of the resonant impedance matching enabling high SNR measurements.

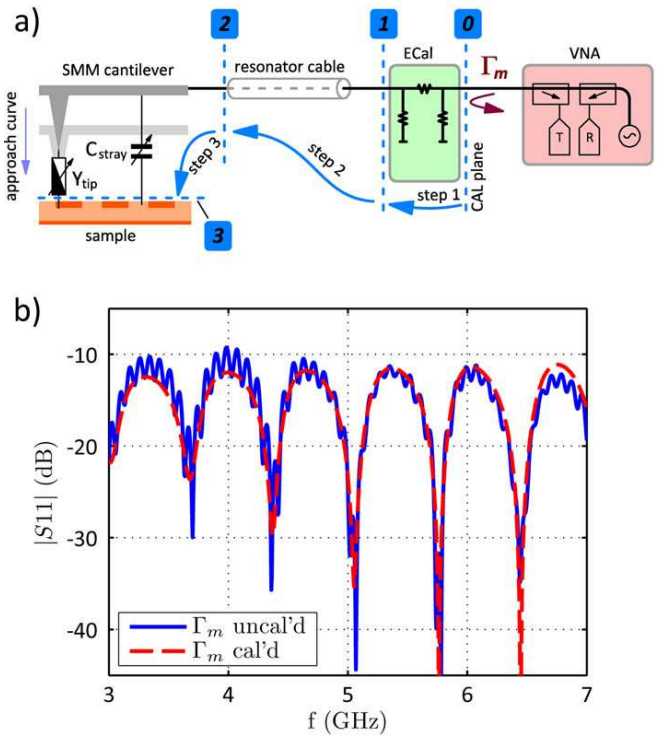

Fig. 1. (a) Overview of system setup including VNA, ECal, resonator cable and actual SMM cantilever scanning on sample surface. Sequential moving of the calibration plane (dashed) towards the cantilever tip. (b) Measured reflection coefficient Γ_m as a function of frequency before (blue) and after (red, dashed) reflection calibration at position 0 in the calibration workflow in (a). Systematic VNA error and the effect of the connection cable cause significant ripple which is removed after this preparative calibration step.

In a preparative step the ECal is used to bring the calibration plane to its port 1 connector (Fig.1 Pos. 0) ensuring proper VNA calibration and eliminating connection cable effects in a frequency range from 1 GHz up to 20 GHz. This is based on the VNAs internal calibration procedure and Fig. 1 (b) shows the effect of the calibration in the frequency domain. While the uncalibrated measurment (blue) shows significant closely spaced ripple, which is an effect of standing waves on the connection cable, in the calibrated measurement (red) the ripple is completely removed. The ECal is then switched into "Thru" state establishing the connection between VNA and resonator cable. The Ecal "Thru" state is a well-defined calibration standard with its properties described in a S2P file. In step 1 this fact is used to de-embed its effect shifting the calibration plane to the ECal port 2 (cf. Fig. 1 Pos. 1). The de-embedding process is described in more detail below.

Fig. 2 shows a Smith chart plot of the measured reflection coefficient for the three calibration steps and for a single frequency. Without calibration (Pos 0) the typical SMM working point (orange dot) is close to the matching point in order to provide good SNR. If tip conductance is increasing the working point is moving on a straight path (green arrow) while increasing tip capacitance results a circularly shaped movement. The absolute position and angle of this uncalibrated working point is arbitrary. After calibration step 1 the calibration plane is located in front of the resonator cable (Pos. 1) which means that the remaining system components are tip admittance, parasitic effects like stray capacitance (cf. Fig. 1) and resonator cable. Since the tip admittance is relatively low compared to the system impedance of 50 Ω, the system looks now almost completely reflective except from some cable losses. Increasing tip conductance makes the system less reflective moving the working point towards the matching point. Increasing tip capacitance results in an additional phase delay resulting in CW circular movement around the matching point.

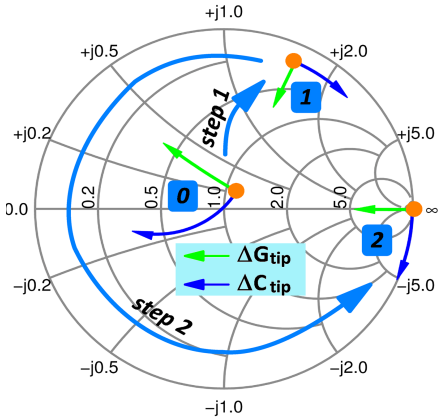

Fig. 2. Sequential calibration steps in the Smith Chart. Starting from a working point close to the matched condition which is typical for SMM (0), the cal plane is moved in front of the resonator cable (1). The remaining phase delay and cable losses are elimiated in step 2 so that the result is an open resonse. Changes in tip conductance and capacitance are indicated by green and blue arrows respectively.

III. Time Domain Gating and De-embedding

Calibration step 2 should remove the effect of the resonator cable and bring the working point to the "open" point. It is convenient for this step to place the tip on the sample surface in order to avoid changes in stray capacitance. The system reflection Γ_{in} is then measured in a 1 GHz–20 GHz frequency range with a sufficient number of points in order to allow time domain transformation by the VNAs built in capabilities (cf. Fig. 3 (b), red trace). Comprehensive information on this is given in [17].

Fig. 3 (a) shows the magnitude of the reflection coefficient in the time domain in linear units. At 100 ps small reflections coming from the ECal–resonator cable transition occur while the main reflection from the actual tip is centered at 3 ns. At 5.8 ns second order reflections travelling between tip and ECal can be identified. It is assumed that these second order

reflections are constant. Subsequently the tip reflection is removed by gating (Fig. 3 (a) dashed line) effectively disconnecting the tip and its parasitics and replacing it by Γext = 0 (cf. Fig. 4). The result is transferred back into frequency domain representing all the small discontinuities (cf. Fig. 3 (b), green trace).

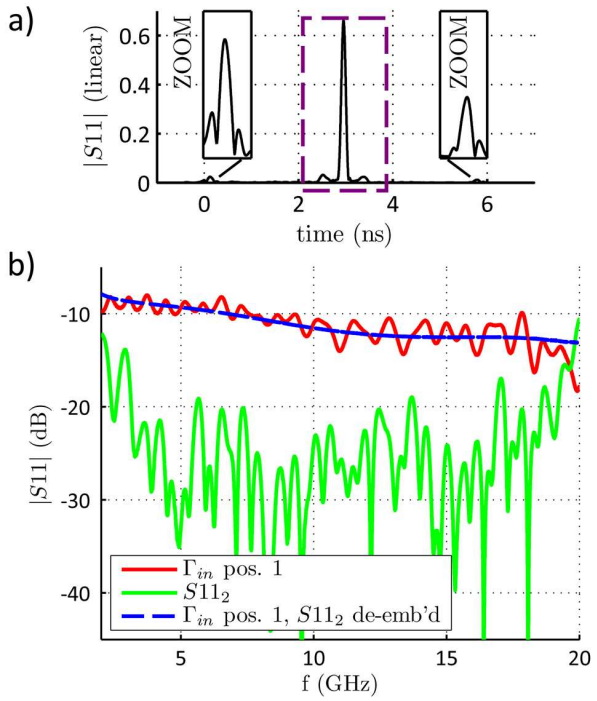

Fig. 3. (a) Time domain transformed system reflection coefficient after calibration step 1. Early reflections at 100 ps are generated by the transition between ECal and cable. The main reflection generated by the SMM tip is centered arround 3 ns and is removed by the gate (dashed). Just before 6 ns a second order reflection can be seen. (b) Magnitude of system reflection coefficient after calibration step 1 in the frequency domain. The red trace includes the tip reflection and all discontinuities while the green trace shows only the discontinuities with removed (gated) tip reflection. Finally the blue trace shows the system response after de-embedding the discontinuities.

Fig. 4 shows how error boxes, each representing a calibration step, are arranged in series. Error box 1 represents the Ecal "Thru" state from step 1 while *S11₂* in error box 2 is the back transferred gated result from step 2 (cf. Fig 3 (b)). Temporarily *S21₂* = 1 and *S12₂* = 1 is assumed and the combination of error box 1 and error box 2 is de-embedded which is done by converting the S-parameters into ABCD-parameters using

$$A = \frac{(1+S_{11})(1-S_{22})+S_{12}S_{21}}{2S_{21}} \qquad B = Z_0\frac{(1+S_{11})(1+S_{22})-S_{12}S_{21}}{2S_{21}}$$

$$C = \frac{1}{Z_0}\frac{(1-S_{11})(1-S_{22})-S_{12}S_{21}}{2S_{21}} \qquad D = \frac{(1-S_{11})(1+S_{22})+S_{12}S_{21}}{2S_{21}}\ . \quad (2)$$

Each error box is represented by an ABCD-parameter matrix and the series connection is just a matrix multiplication. Moreover multiplying the inverse of the resulting matrix with the measured data results in de-embedding the effects of the error boxes.

Again the system reflection is measured now assuming Γext = 1 and without gating. The response is very similar to a lossy transmission line with nearly linear phase. The measured magnitude in Fig. 3 (b, blue trace) shows some loss increasing with frequency. In fact this result represents the resonator cable and the phase delay coming from the tip and its contacting and is subsequently mapped equally to *S21₂* and *S12₂*. Error box 2 is now completely defined and after including the new error box 2 in the de-embedding process the system response is made equally to an "Open" with |*S11*| = 1 and arg (*S11*) = 0 degree (cf. Fig. 2 Pos 2). Changes in conductivity are mapped now into amplitude and changes in capacitance into phase, respectively.

IV. Complex Impedance Calibration

The last part of the calibration converts the phase-calibrated S_{11} into calibrated capacitance and conductance. This method moves the calibration plane of the Nose Cone connector to the AFM cantilever and works *in situ* on the sample under test, so no calibration sample is required. The calibration procedure is based on the simultaneous acquisition of Electrostatic Force Microscopy (EFM) and S_{11} approach curves in order to calculate the error coefficients of error box 3 (cf. Fig. 4). A low frequency EFM approach curve is used to measure the capacitance change with the distance when the cantilever approaches the sample surface. The relation between electrostatic force, F_{es} and tip-sample capacitance, *C(z)*, is

$$\frac{dC}{dz} = \frac{4F_{es,2\omega}}{V_0^2} \quad (3)$$

where

$$v(t) = V_0 * sin(\omega t) \quad (4)$$

is the exitation voltage and $F_{es,2\omega}$ is the resulting electrostatic force. By integration, *C(z)* is obtained and

$$Z_{tip} = \frac{1}{j\omega C} \overset{yields}{\rightarrow} \Gamma_{tip} = \frac{Z_{tip} - Z_0}{Z_{tip} + Z_0} \quad (5)$$

where Z_0 = 50 Ω is the characteristic system impedance. Finally the relation

$$\Gamma_m = S11_3 + \frac{S21_3 S12_3 \Gamma_{tip}}{1 - S22_3 \Gamma_{tip}} \quad (6)$$

is used to calculate the coefficients of error box 3 (*S11*$_3$, *S21*$_3$, *S12*$_3$, *S22*$_3$). Subsequently all three error boxes are de-embedded effectively shifting the calibration plane to the tip apex.

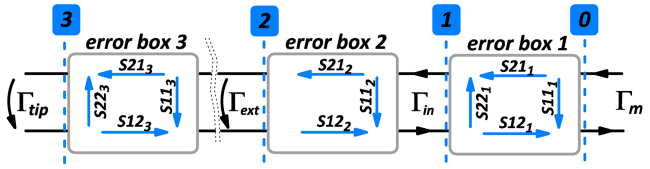

Fig. 4. In order to measure Γ_{tip} it is necessary to deembed three error boxes corresponding to the ECal (error box 1) the resonator cable (2) and tip coupling effects (3).

V. Results

To demonstrate the proposed calibration workflow and its capability to map the conductance and capacitance to the S11 amplitude and phase, respectively, a doped silicon sample with gold dot electrodes residing on silicon oxide was measured. Fig. 5(a) shows the cross section of the sample on the left and the corresponding AFM measured topography on the right. The different dot sizes (1 µm, 2 µm, 3 µm and 4 µm) and oxide thicknesses (50 nm, 100 nm, 150 nm and 200 nm) provide different capacitance values (~ 100 aF – 8.8 fF). In addition, some gold dot electrodes are placed directly on the doped silicon effectively forming nano-Schottky diodes. If the diodes are biased in forward and reverse direction their conductivity can be influenced as previously shown in [18]. The DC bias voltage is applied through the cantilever and its associated RF connection in combination with a bias-tee. For precise bias control a source meter unit (Keysight B2902) was used. The return path for the DC bias is established by the grounded silicon substrate. Fig. 5(b) shows the measured reflection coefficient after calibration for reverse bias. The various capacitances including the Schottky diodes can be seen in the phase image on the right. The amplitude image on the left shows constant 0 dB reflection for the whole sample indicating purely reactive behavior. In the forward biased case which is shown in Fig. 5(c) the phase has changed slightly for some of the MOS capacitors indicating varactor behavior. The phase and therefore the capacitance of the Schottky diodes remains almost unchanged. In the amplitude image the Schottky diodes can be seen as bright spots indicating decreased reflection which corresponds to lossy behavior. Both measurements were done at 6 GHz.

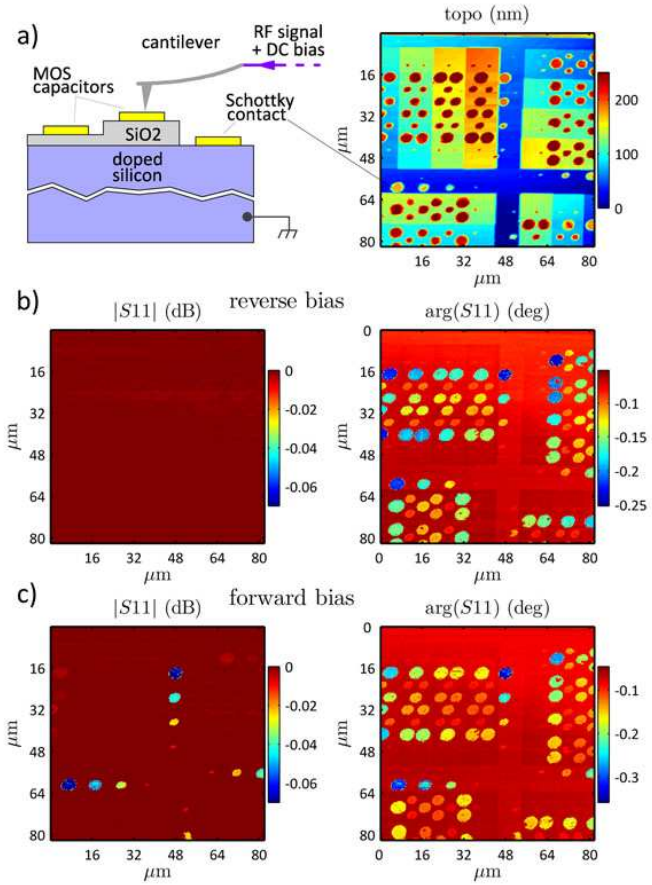

Fig. 5. (a) The cross section of the measured sample is shown in the sketch on the left. Gold electrodes residing on SiO2 steps form MOS capacitors while electrodes placed directly on the substrate form nano Schottky diodes. On the right the AFM measured topography is shown. Scansize is 80 x 80 µm² and the SiO2 stepheight is approximately 50 nm. (b) Amplitude and phase data for measured nanoscopic MOS capacitors and Schottky diodes in reverse bias after calibration step 2. Purely reactive sample behavior is indicated since only the phase changes during the scan while the amplitude remains at 0 dB. (c) Forward bias is applied to the Schottky diodes resulting in a conductive (lossy) behavior which is indicated by a decreased amplitude.

To obtain fully quantified capacitance and conductance data as shown shown in Fig. 6 an additional calibration step based on AFM-tip approach curves was performed (cf. section III; [15]). The additional calibration step removes the effect of parasitic stray capacitances and establishes a correct scale of both conductance and capacitance. The combination of the phase calibration and the amplitude calibration with approach curves is a robust and advanced SMM complex impedance calibration workflow. Figure 6 shows that the parallel conductance of the forward biased Schottky diodes is in the range of roughly 0.1 mS – 1 mS while the MOS capacitors show no significant signal. The capacitance of the MOS capacitors is, depending on the capacitor surface area and dielectric thickness, well within the expected range of

100 aF – 8.8 fF, with the forward biased Schottky diodes showing similarlyhigh capacitances.

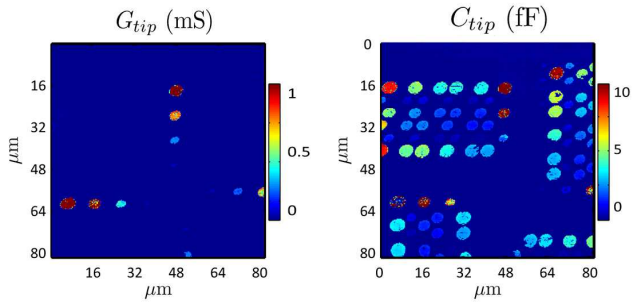

Fig. 6. An additional calibration step involving AFM tip-approach curves enables fully calibrated measurement of conductance (in units of milli-Siemens) and capacitance (in units of femto-Farad). AFM-tip approach curves effectively generate variable and known capacitances that are used as calibration capacitances. Both images are basically scaled versions of the corresponding amplitude and phase images in Fig. 5 (c).

Also biological samples can be investigated with the proposed method. Fig. 7 shows the phase calibrated measurement of ARPE-19 (Arising Retinal Pigmented Epithelia) cells at 8.42 GHz. The cells were dried and chemically fixed on a conductive silicon substrate with the measurement done in air. In Fig. 7(a) the topographical image is shown at a scan size of 36 um x 36 um. The topographical measurement was corrected for sample tilting by subtracting a linear plane. The overall cell height is up to 1µm while the lateral cell diameter is roughly 5 µm – 7 µm. In Fig. 7(b) the corresponding amplitude and phase image of the measured reflection coefficient is shown after calibration step 2. For calibration, the tip was placed on the substrate. In the amplitude image there is almost no signal difference between cell and substrate indicating low losses of the dried cells. Since water is mostly removed due to the drying process and the imaging in air, also the corresponding conductivity coming from water within the cell and surrounding the cell is reduced. This is in line with previous SMM measurements done at different humidity levels [6]. The phase image shows a strong contrast according to variations in capacitance. The values are relative with respect to the substrate and positive phase values correspond to lower capacitance values. As shown in a recent study [7], variations in the cell capacitance are typically coming from different dielectric behavior of cell compartments with different chemical composition and density. As such the calibrated phase image is sensitive to biologically relevant information of the cell interior.

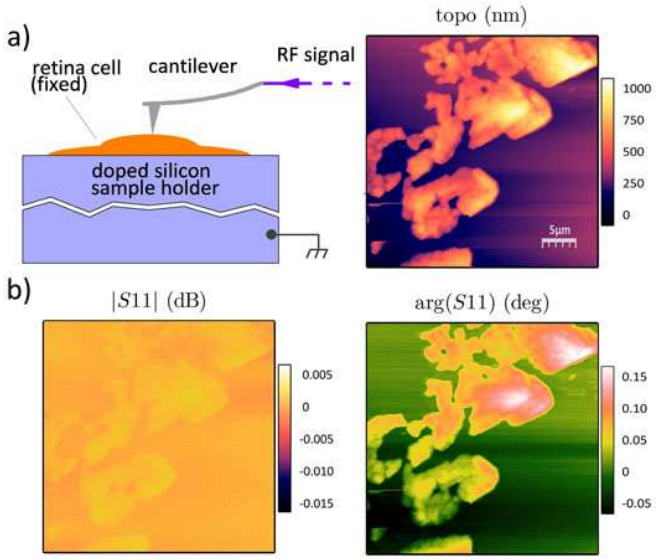

Fig. 7. (a) Sketch of biological cell measurements in air. ARPE-19 cells are placed on a conductive silicon substrate and are imaged with the SMM. The topography is shown with a scan size of 36 µm x 36 µm. (b) Amplitude and phase of S11 reflection coefficient after calibration step 2 measured at 8.42 GHz. During calibration the tip was placed on the substrate. The amplitude image shows almost no contrast indicating low losses in the dried and chemically fixed cells. The phase image shows strong contrast corresponding to variations in capacitance and dielectric properties.

VI. Conclusion and Outlook

A new calibration workflow has been developed to accurately determine the conductivity and capacitance from the S11 reflection coefficient amplitude and phase, respectively, without the need of nanoscale calibration standards. In contrast to other calibration workflows, the developed procedure calibrates the entire frequency range of the SMM (e.g. 1-20 GHz), such that the SMM measurement frequency can be easily changed during imaging. This makes it ideal to study frequency dependent effects of materials including semiconductor dopant profiling and subsurface imaging of buried structures at different skin depths. The final step of the calibration workflow is based on the SMM cantilever approach curve resulting in quantitative conductance and capacitance images with nanoscale resolution. The new method is expected to have applications for semiconductor dopant calibrations, advanced materials science measurements, and accurate dielectric capacitance measurements of biological samples including bacteria and living cells. The calibration workflow presented here allows to determine more accurately the doping density and depletion layer capacitance in semiconductor samples, the conductivity of advanced materials including graphene, and the dielectric properties of cell compartments and biomolecular water hydration at broadband 1-20 GHz frequencies.

ACKNOLEDGEMENT

The authors would like to thank Lilia Chtcheglova and Silviu Tuca from Johannes Kepler University of Linz for cell sample preparation. This work has been supported by EU FP7 (PEOPLE-2012-ITN-317116, NANOMICROWAVE), Bio-SMM FFG (Project No. 846532), and FWF Project P 28018-B27.

REFERENCES

[1] A. Gregory et al., "Measurement of the permittivity and loss of high-loss materials using a Near-Field Scanning Microwave Microscope," in *84th Microwave Measurement Conference (ARFTG)* , Boulder, CO, 2014, pp. 1-8.

[2] E. Brinciotti et al., "Probing resistivity and doping concentration of semiconductors at the nanoscale using scanning microwave microscopy," *Nanoscale*, vol. 7, no. 35, pp. 14715-14722, 2015.

[3] A. Imtiaz et al., "Frequency-selective contrast on variably doped p-type silicon with a scanning microwave microscope," *J. Appl. Phys.*, vol. 111, no., p. 093727, 2012.

[4] H. P. Huber et al., "Calibrated nanoscale dopant profiling using a scanning microwave microscope," *J. Appl. Phys.*, vol. 111, no. 1, p. 014301, 2012.

[5] Y. J. Oh et al., "High-frequency electromagnetic dynamics properties of THP1 cells using scanning microwave microscopy," *Ultramicroscopy*, vol. 111, pp. 1625-1629, 2011.

[6] S. S. Tuca et al., "Calibrated complex impedance of CHO cells and E . coli bacteria at GHz frequencies using scanning microwave microscopy," *Nanotechnology*, vol. 27, no. 13, p. 135702, 2016.

[7] M. C. Biagi et al., "Nanoscale Electric Permittivity of Single Bacterial Cells at Gigahertz Frequencies by Scanning Microwave Microscopy," *ACS Nano*, vol. 10, no. 1, pp. 280-288, 2016.

[8] G. Gramse et al., "Quantitative sub-surface and non-contact imaging using scanning microwave microscopy," *Nanotechnology*, vol. 26, no. 13, p. 135701, 2015.

[9] C. Plassard et al., "Detection of defects buried in metallic samples by scanning microwave microscopy," *Physical Review*, vol. 83, no. 11, p. 121409, 2011.

[10] T. Dargent et al., "An interferometric scanning microwave microscope and calibration method for sub-fF microwave measurements," *Rev. Sci. Instrum.*, vol. 84, no. 12, p. 123705, 2013.

[11] A. Imtiaz et al. "Near-field scanning microwave microscopy: An Emerging Research Tool for Nanoscale Metrology," IEEE Microw. Mag., vol. 15, no. 1, pp. 52-64, 2014.

[12] J. Hoffmann et al., "A Calibration Algorithm for Nearfield Scanning Microwave Microscopes," in *12th IEEE Int. Conf. Nanotechnology*, Birmingham, 2012, p. 4.

[13] H. P. Huber et al., "Calibrated nanoscale capacitance measurements using a scanning microwave microscope," *Rev. Sci. Instrum.*, vol. 81, no. 11, p. 113701, 2010.

[14] M. Farina et al., "Calibration Protocol for Broadband Near-Field Microwave Microscopy," *IEEE Trans. Microw. Theory Tech.*, vol. 59, no. 10, pp. 2769-2776, 2011.

[15] G. Gramse et al., "Calibrated complex impedance an permittivity measurements with scanning microwave microscopy," *Nanotechnology*, vol. 25, no. 14, p. 145703, 2014.

[16] Keysight Technologies. (2002). *Applying Error Correction to Network Analyzer Measurements* [Online].

[17] Keysight Technologies. (2012). *Time Domain Analysis Using a Network Analyzer* [Online].

[18] M. Kasper et al., "Metal-oxide-semiconductor capacitors and Schottky diodes studied with scanning microwave microscopy at 18 GHz," *J. Appl. Phys.*, vol. 116, no. 18, p. 184301, 2014.